Supporting Information

Superior-Performance Lithium-Sulfur Battery: Face-Centered-Cubic-Structure High-entropy Alloy Improves the Bidirectional Catalytic Conversion of Polysulfide/Sulfide

Xueyu Wang[+], Peirong Lin[+], Chuanhuang Wu, Yuchuan Zhu, Cong Wang, Daying Guo*, Xi'an Chen*, and Shun Wang*

Key Laboratory of Carbon Materials of Zhejiang Province, College of Chemistry and Materials Engineering, Wenzhou University, Wenzhou, China 325035.

* To whom correspondence should be addressed. E-mail: guody@wzu.edu.cn; xianchen@wzu.edu.cn; shunwang@wzu.edu.cn

+ These authors contributed equally to this work.

EXPERIMENTAL SECTION

Preparation of rGO@S cathode: The rGO@S composites were prepared by the melt diffusion method. Typically, rGO@S material was fabricated by grinding sulfur and carbon nanotube (3:7, weight ratio), and heated at 155 °C for 12 hours. 80% rGO@S, 10% Super P, and 10% PVDF were combined in NMP solvent to get a homogeneous slurry. After coating on aluminum foil using a 200 μm applicator, the slurry was dried overnight in vacuum at 60 °C. The sulfur loading on the electrode sheet accounted for about 0.8-1.2 mg cm^{-2}. In addition to this, cathodes with a sulfur loading of about 4.4 mg cm^{-2} were prepared and used to test the electrochemical performance at high loadings.

Li$_2$S nucleation test: The Li$_2$S nucleation test was conducted to study the conversion kinetics of the liquid-solid process. CoNiCuMnMo-HEA@rGO in NMP configuration into slurry, uniform drop on carbon cloth, drying as cathode material. S and Li$_2$S were continuously stirred in TGDME at a molar ratio of 7:1 to obtain 0.2 M solution of Li$_2$S$_8$ as electrolyte. PP film as separator, lithium metal as anode. The assembled cells were discharged to 2.06 V at 0.112 mA and then potentiostatically discharged until the current dropped below 10^{-5} A at 2.05 V.

Li$_2$S dissociation test： The Li$_2$S dissociation test follows the same cell assembly process as the nucleation test. Then, the current of 0.112 mA is constant discharge to 2.20 V, and switch to 2.0 V for potentiostatic discharge test. Then, 0.112 mA charged the battery to 2.20 V, and switched to 2.4 V for constant potential charging test.

Material and performance characterization

Topography is done by (FEI Quanta 650 field emission (FE)-SEM). TEM and HRTEM images and corresponding EDS element mappings were taken on a transmission electron microscope (TEM, JEM-2100F) instrument. The S content in the rGO@S cathode is measured by thermogravimetric analysis (TGA) on the

Dimond PE analysis system, provides that it is done Heating from 40 °C to 800 °C at a heating rate of 10 °C min^{-1} under nitrogen atmosphere. X-ray photoelectron spectrometer (XPS) analysis is performed via Thermo Fisher Scientific K-Alpha. Polysulfide adsorption experiments are tested by a liquid UV-Vis spectrophotometer (UV-1800) in the wavelength range of 200-800 nm.

Theoretical calculations

The Vienna Ab Initio Package (VASP) was employed to perform all the density functional theory (DFT) calculations within the generalized gradient approximation (GGA) using the Perdew, Burke, and Enzerh of (PBE) formulation.[1-3] The projected augmented wave (PAW) potentials were applied to describe the ionic cores and take valence electrons into account using a plane wave basis set with a kinetic energy cutoff of 450 eV.[4,5] Partial occupancies of the Kohn–Sham orbitals were allowed using the Gaussian smearing method and a width of 0.05 eV. The electronic energy was considered self-consistent when the energy change was smaller than 10^{-5} eV. A geometry optimization was considered convergent when the force change was smaller than 0.03 eV/Å. Grimme's DFT-D3 methodology was used to describe the dispersion interactions.[6] The vacuum spacing perpendicular to the plane of the structure is 20 Å. The Brillouin zone integral utilized the surfaces structures of 2×2×1 monkhorst pack K-point sampling. Finally, the adsorption energies (E_{ads}) were calculated as E_{ads}= $E_{ad/sub}$-E_{ad}-E_{sub}, where $E_{ad/sub}$, E_{ad}, and E_{sub} are the total energies of the optimized adsorbate/substrate system, the adsorbate in the structure, and the clean substrate, respectively. The free energy was calculated using the equation:

$$G = E + ZPE - TS$$

where G, E, ZPE and TS are the free energy, total energy from DFT calculations, zero point energy and entropic contributions, respectively.
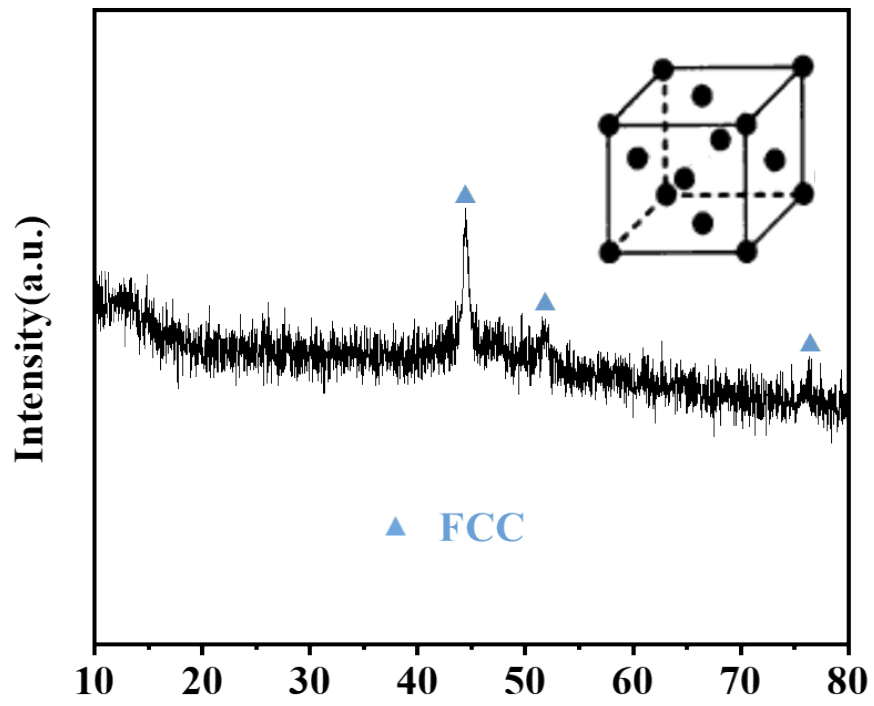
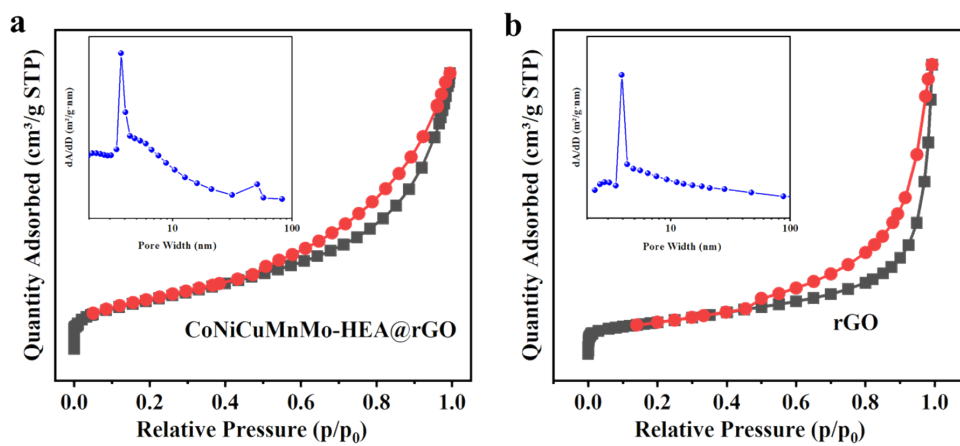**Figure S1.** XRD analysis of the composite CoNiCuMnMo-HEA@rGO,

Figure S2. N_2 adsorption-desorption isotherm and pore size distributions of (a) CoNiCuMnMo-HEA@rGO and (b) rGO.
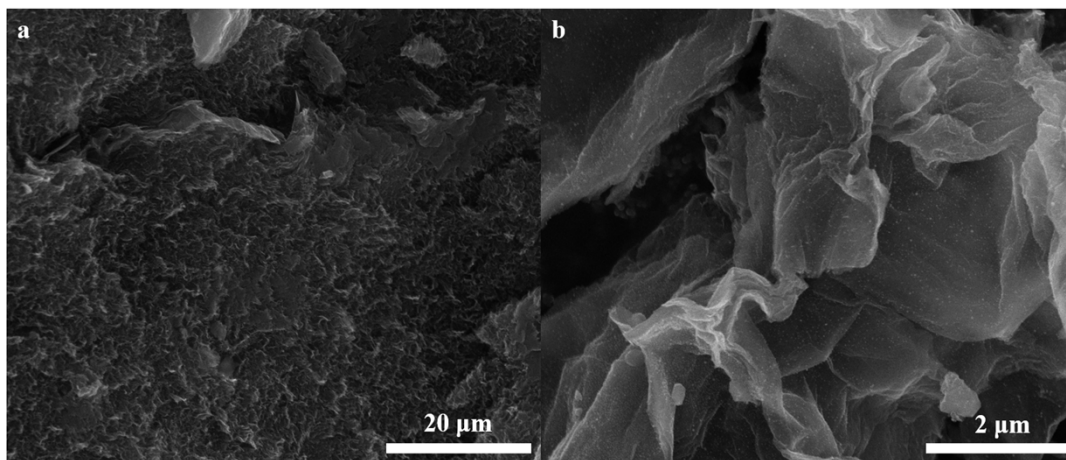
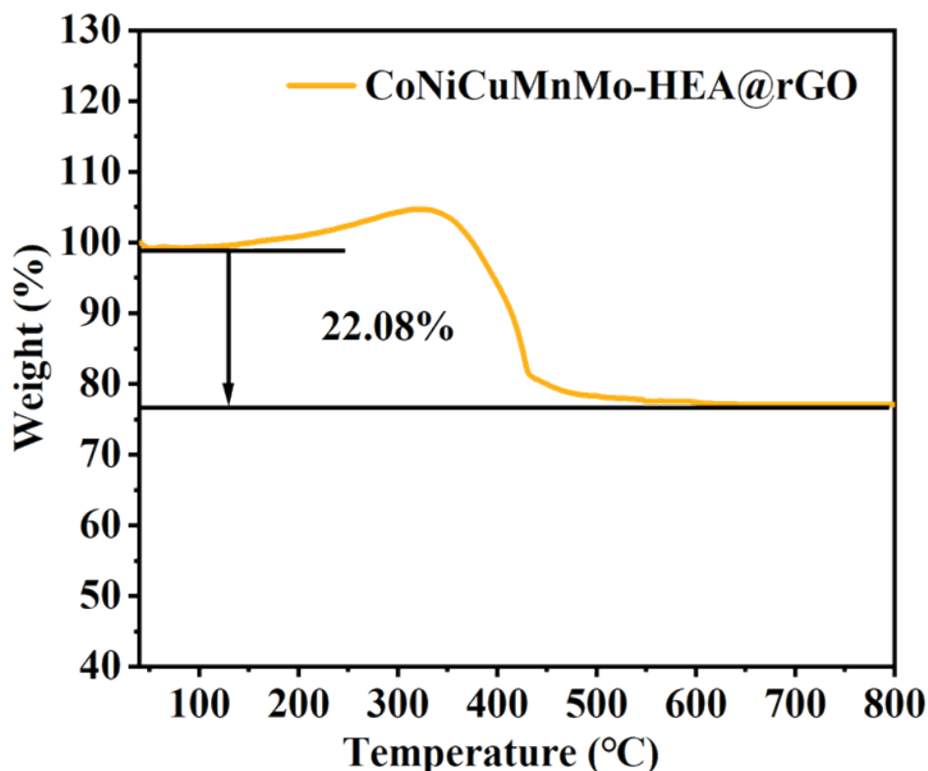**Figure S3.** SEM image of CoNiCuMnMo-HEA@rGO.

Figure S4. TGA curve of the CoNiCuMnMo-HEA@rGO under air at a heating rate of 10 °C/min from 40 °C to 800 °C.

In the TGA analysis of CoNiCuMnMo-HEA@rGO, in the temperature range of 100-800 °C, there are two processes that occur. One is the combustion process of the graphene, so the weight of graphene in the composite would be completely removed from the composite after the TGA heating in air to 800°C. Another is the oxidation process of CoNiCuMnMo (CoNiCuMnMo + O_2 → CoNiCuMnMoO$_{15}$), so the weight of oxygen in the sample would be increased. The tendency to shift towards higher mass at 200-350 °C is attributed to the adsorption of oxygen by the metal to generate oxides, while the gasification temperature of graphene has not yet been reached.Therefore, the final residue of the composite is only CoNiCuMnMoO$_{15}$ after the TGA heating in air to 800 °C. The content of CoNiCuMnMo in the composite was determined based on the following Equation (S1) :

$$CoNiCuMnMo \ (wt\%)$$
$$= 100\% \times \frac{molecular \ weight \ of \ CoNiCuMnMo}{molecular \ weight \ of \ CoNiCuMnMoO_{15}} \times \frac{final \ weight \ of}{initial \ weight \ of \ CoN}$$

(S1)

The final residue content of SnO2 for the CoNiCuMnMo-HEA@rGO sample after the heating in air to 800 oC was 87.92% (Figure S4). The Sn content in the CoNiCuMnMo-HEA@rGO sample was 65.04%, calculated based on Equation (S1):

$$CoNiCuMnMo \ (wt\%) = \frac{332.06}{572.045} \times 87.92\% = 51.04\%$$

In **Figure S5b**, the peaks at 228.50 and 230.06 eV are attributed to Mo^0 $3d_{5/2}$ and Mo^0 $3d_{3/2}$. The peaks at 232.27, 233.94, 235.48 and 237.02 eV correspond to Mo^{4+} $3d_{5/2}$, Mo^{6+} $3d_{5/2}$, Mo^{4+} $3d_{3/2}$ and Mo^{6+} $3d_{3/2}$, respectively. In the high-resolution copper 2p spectrum (**Figure S5c**), two peaks with binding energies of 932.78 and 952.28 eV correspond to Cu^0 $2p_{3/2}$ and Cu^0 $2p_{1/2}$ respectively, and the peaks of 934.83 and 954.58 eV correspond to Cu^{2+} $2p_{3/2}$ and Cu^{2+} $2p_{1/2}$ respectively. In **Figure S5d,** the peaks at 778.63 and 797.48 eV correspond to Co^0 $2p_{3/2}$ and Co^0 $2p_{1/2}$, respectively. The peaks of 781.33 and 801.04 eV are attributed to Co^{2+} $2p_{3/2}$ and Co^{2+} $2p_{1/2}$, and the satellite peaks are 787.78 and 805.13 eV. The peaks at 852.88 and 873.68 eV can be attributed to Ni^0 $2p_{3/2}$ and Ni^0 $2p_{1/2}$. The peaks at 856.03 and 878.08 eV can be attributed to Ni^{2+} $2p_{3/2}$ and Ni^{2+} $2p_{1/2}$. The peaks at 861.83 and 881.28 eV belong to satellite peaks (**Figure S5e**). As shown in **Figure S5f**, the proportion of various metals and surfaces oxidized by air to form metal oxides. Mn is the most oxidized element, indicating its high catalytic activity.
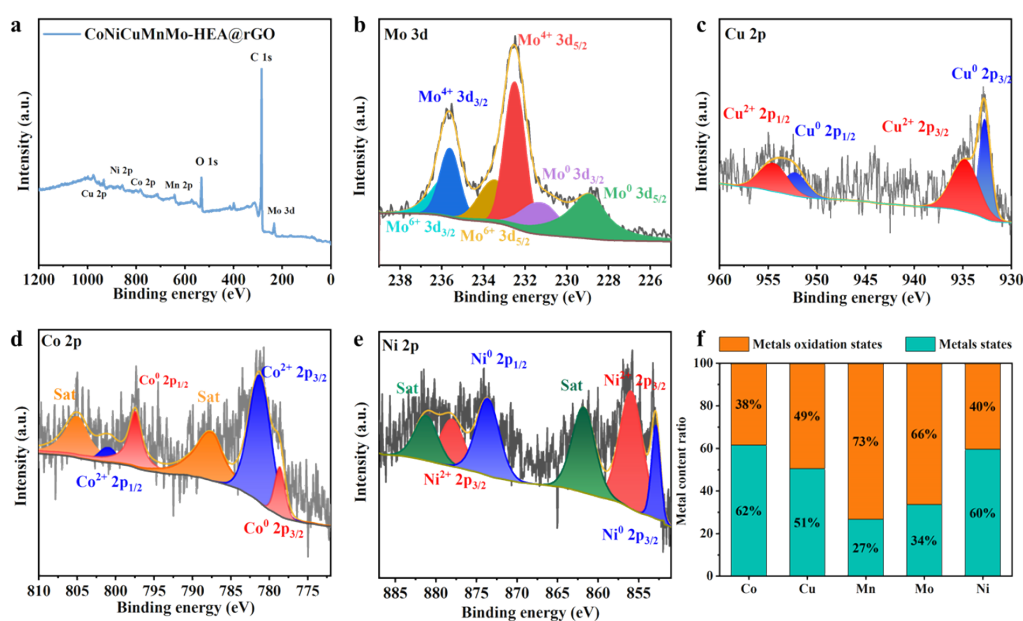

Figure S5. (a) Fine XPS spectral, (b) Mo 3d, (c) Cu2p, (d) Co 2p and (e) Ni 2p analysis of CoNiCuMnMo-HEA@rGO. (f) The proportion of various metals and surfaces oxidized by air to form metal oxides.
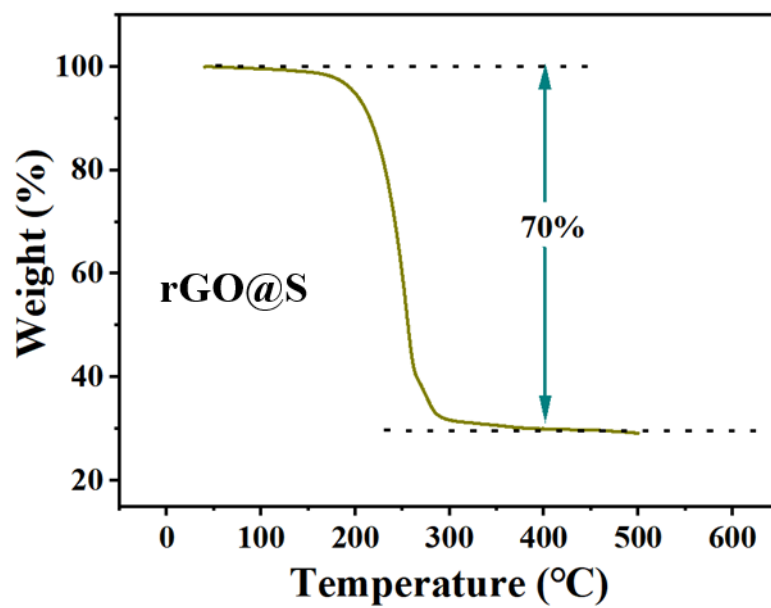
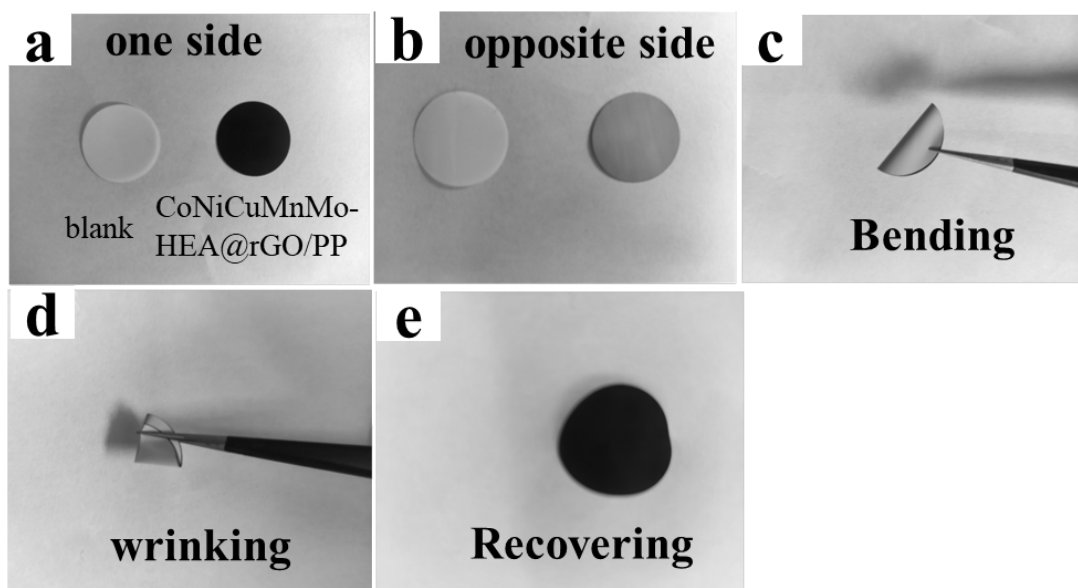**Figure S6.** Thermogravimetric analysis of the rGO@S cathode.

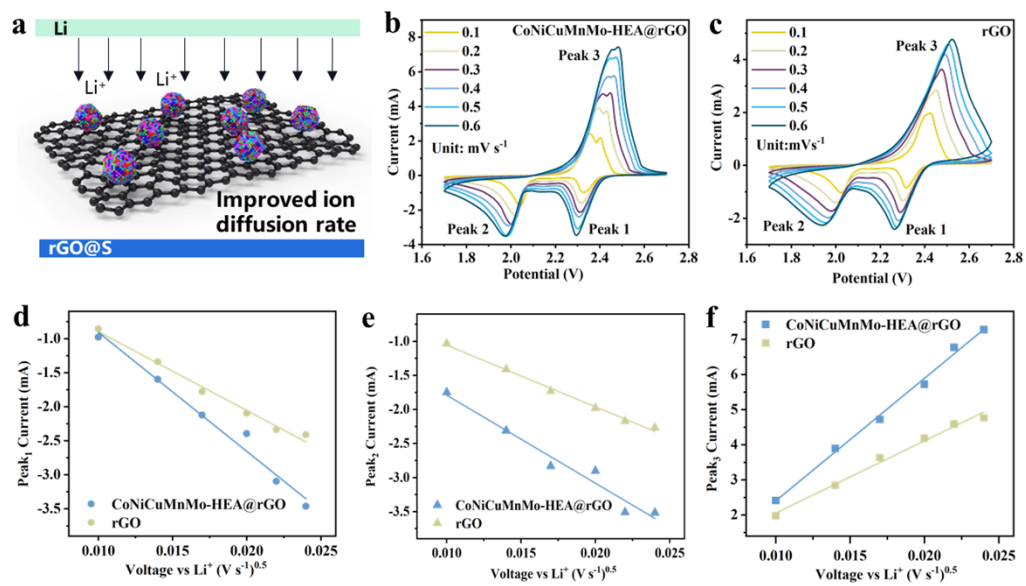**Figure S7**. Folding and recovering test CoNiCuMnMo-HEA@rGO/PP coating adhesion.

Figure S8. Comparison of Li$^+$ diffusion behavior. (a) Schematic diagram of ion diffusion rate in battery. Battery CVs taken at multiple scan rates of (b) CoNiCuMnMo-HEA@rGO and (c) rGO. (d-f) Randles−Sevcik plots of peak current vs the square root of the scan rate for the two cathodic and anodic redox peaks.
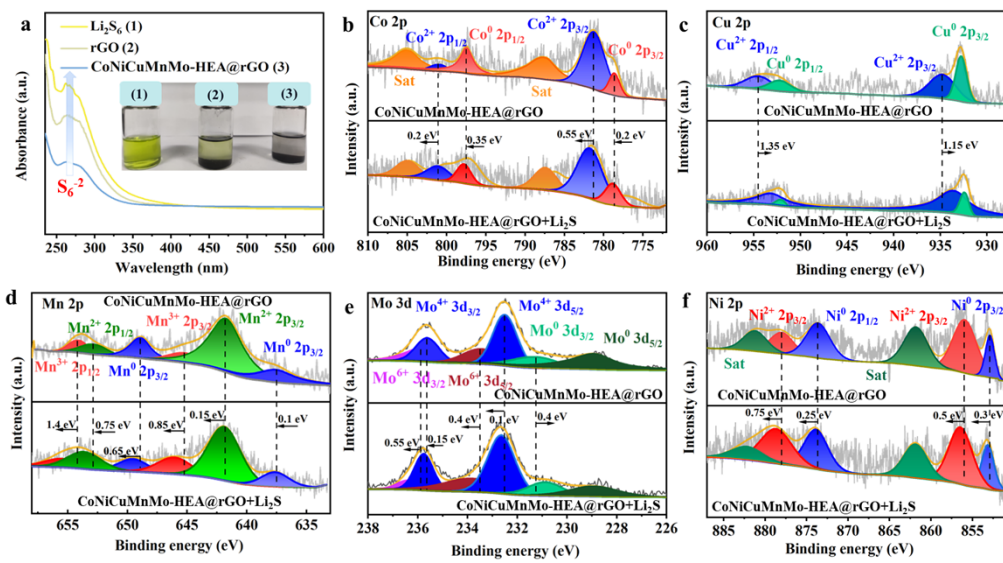
Figure S9. (a) Uv–vis spectra and optical photographs of different samples in contact with Li_2S_6. XPS spectrum of (b) Co 2p, (c) Cu 2p, (d) Mn 2p, (e) Mo 3d and (f) Ni 2p for CoNiCuMnMo-HEA@rGO before and after adsorbed Li_2S_6.
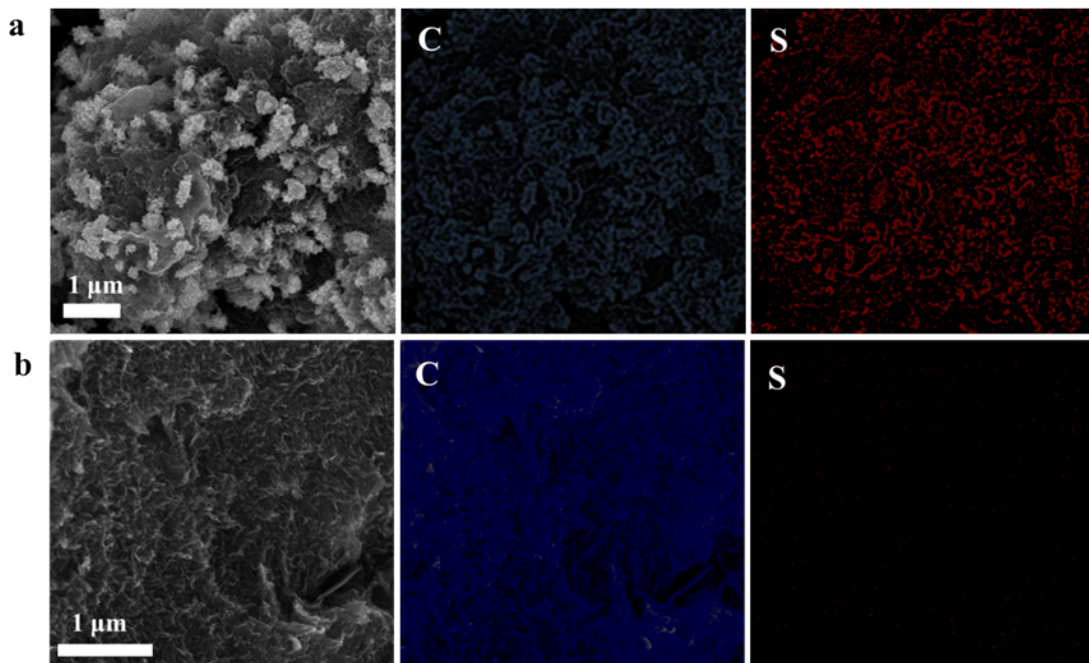
Figure S10. Ex situ SEM and C, S elemental mapping images of S@rGO electrodes containing (a) CoNiCuMnMo-HEA@rGO/PP and (b) rGO/PP separators during discharge.
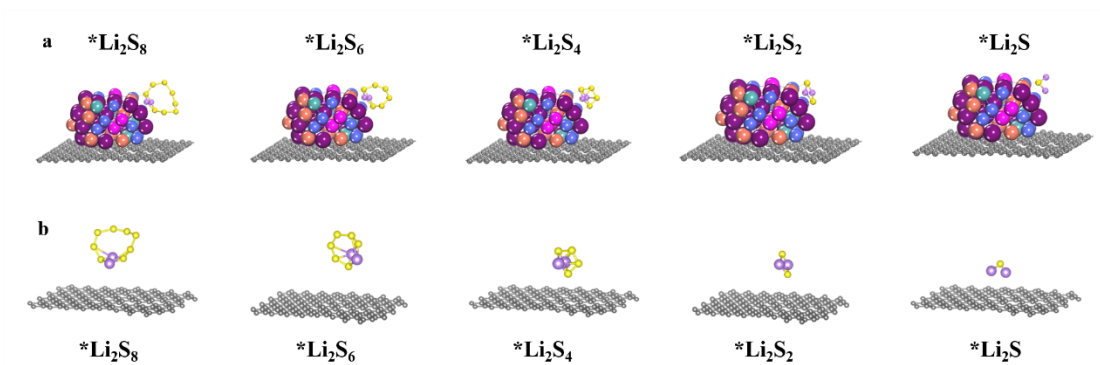
Figure S11. Structural models of adsorption of *Li$_2$S$_8$, *Li$_2$S$_6$, *Li$_2$S$_4$, *Li$_2$S$_2$, *Li$_2$S on (a) CoNiCuMnMo-HEA@rGO and (b) rGO surfaces.
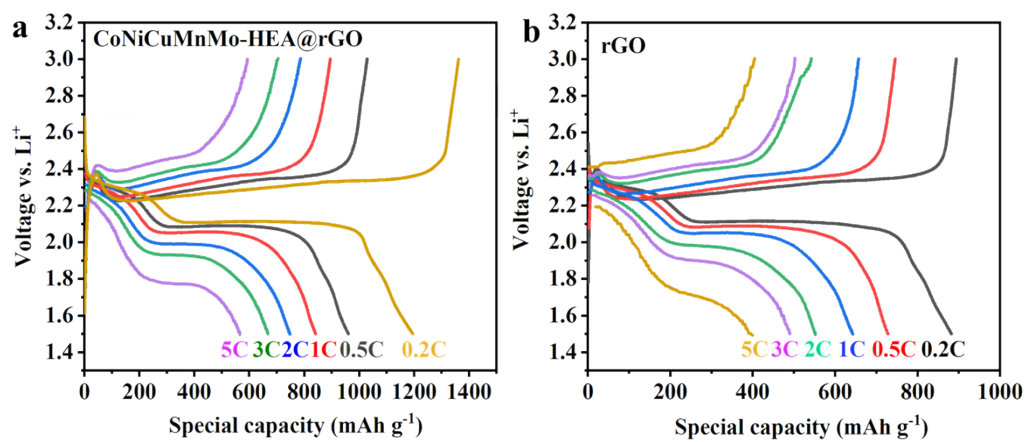
Figure S12. Constant current charge/discharge curve of (a) CoNiCuMnMo-HEA@rGO/PP and (b) rGO/PP.
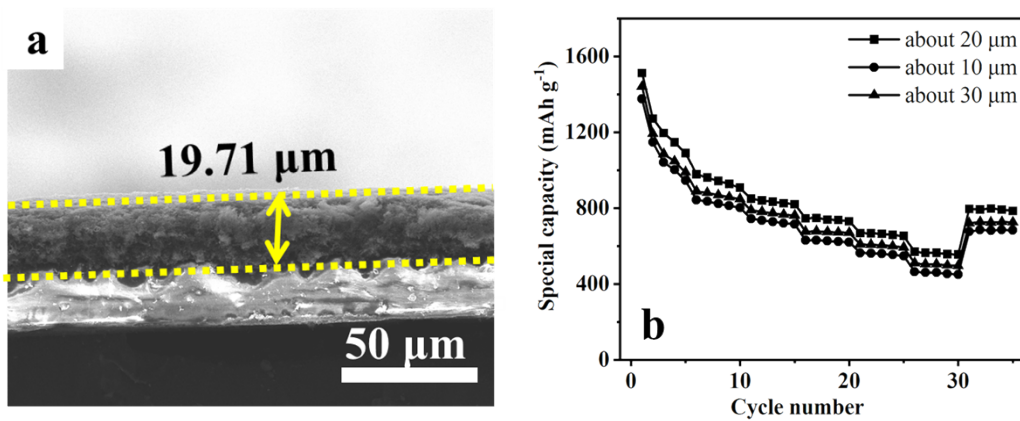
Figure S13. (a) Cross-sectional SEM image of CoNiCuMnMo-HEA@rGO separator. (b) Multiplication performance of CoNiCuMnMo-HEA@rGO cell with different coating thicknesses.
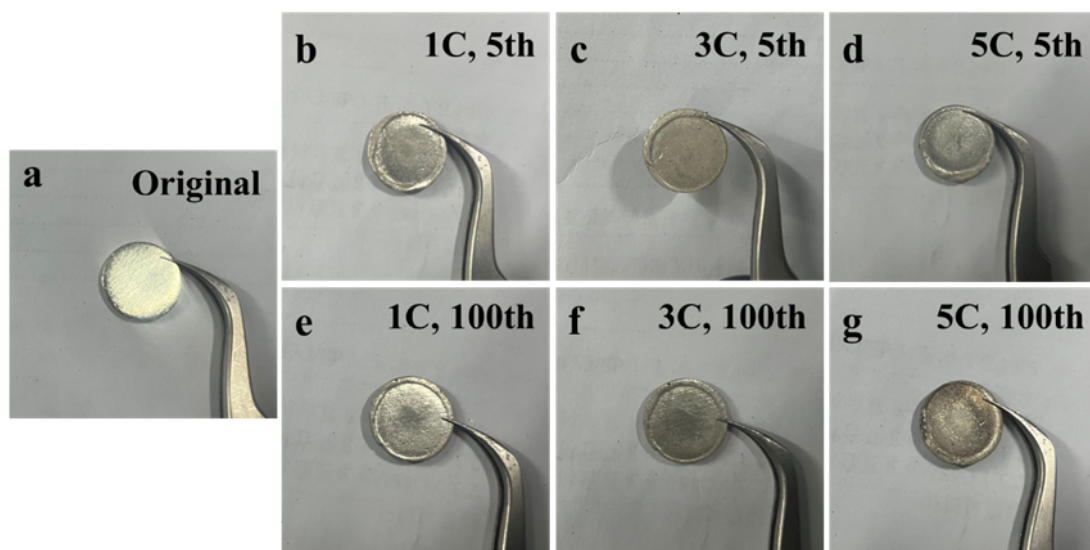
Figure S14. The optical photographs of lithium metal electrodes after cycling at different rates (1C, 3C, 5C), which have been washed thoroughly with anhydrous DME solvent.
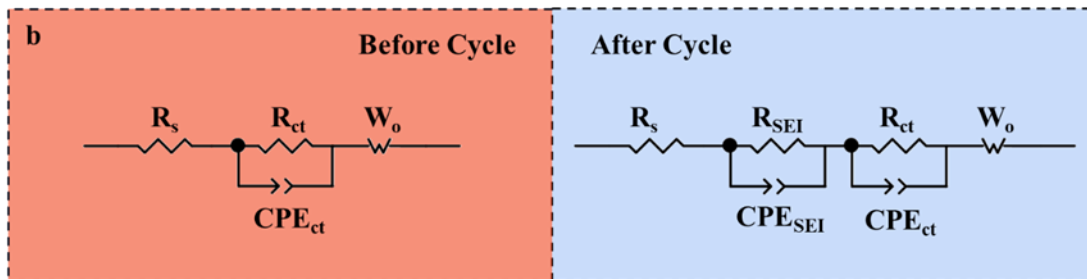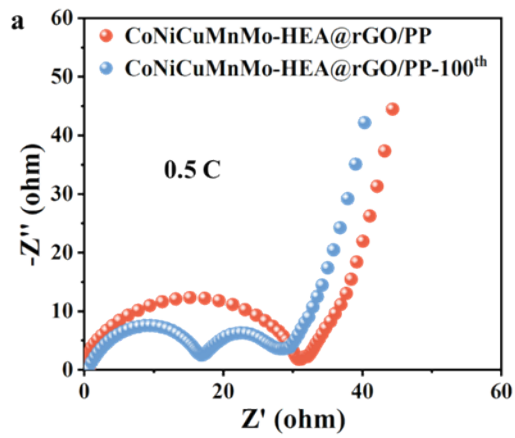
Figure S15. (a) Nyquist plots before and after 100 cycles of the battery having the CoNiCuMnMo-HEA@rGO/PP. (b) Equivalent circuit models of the battery with the CoNiCuMnMo-HEA@rGO/PP before and after 100 cycles.
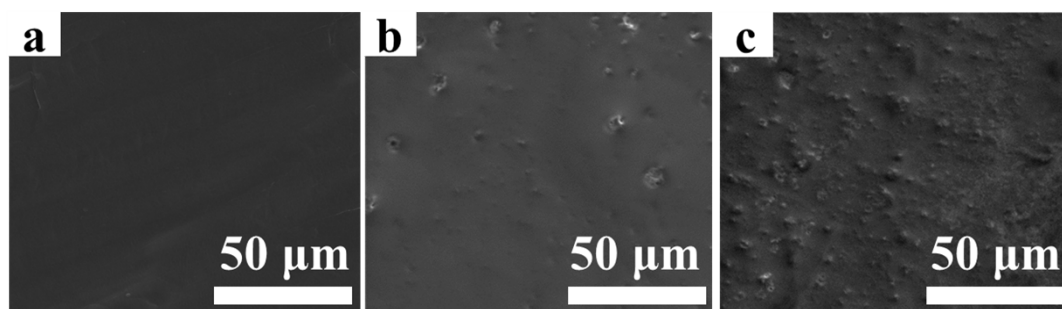
Figure S16. (a) SEM images of pure Li surface. SEM images of anode surface of the (b) CoNiCuMnMo-HEA@rGO and (c) rGO after 100 cycles.

Table S1. The rate performance (mAh g^{-1}) of CoNiCuMnMo-HEA@rGO/PP and rGO/PP cells.

Capacity (mAh g^{-1}) Rate / Sample	0.2 C	0.5 C	1 C	2 C	3 C	5 C	0.2 C
CoNiCuMnMo-HEA@rGO/PP	1512.4	979	850	746.7	669	570.2	796.5
rGO/PP	883.8	718.2	596.5	510.3	455.9	397.6	635.8

Reference

[1] G. Kresse, J. Furthmüller, Efficient Iterative Schemes for Ab Initio Total-Energy Calculations Using a Plane-Wave Basis Set. *Phys. Rev. B*, 1996, **54**, 11169–11186.

[2] J. P. Perdew, K. Burke, M. Ernzerhof, Generalized Gradient Approximation Made Simple. *Phys. Rev. Lett.*, 1996, **77**, 3865–3868.

[3] G. Kresse, D. Joubert, From Ultrasoft Pseudopotentials to the Projector Augmented-Wave Method. *Phys. Rev. B*, 1999, **59**, 1758-1775.

[4] P. E. Blöchl, Projector Augmented-Wave Method. *Phys. Rev. B*, 1994, **50**, 17953–17979.

[5] S. Grimme, J. Antony, S. Ehrlich, H. J. Krieg, *Chem. Phys.*, 2010, **132**, 154104.

[6] G. Henkelman, B. P. Uberuaga, H. J. Jonsson, *Chem. Phys.*, 2000, **113**, 9901.